


Article

Measuring Vegetation Phenology with Near-Surface Remote Sensing in a Temperate Deciduous Forest: Effects of Sensor Type and Deployment

Fan Liu ^{1,2}, Xingchang Wang ^{1,2,*} and Chuankuan Wang ^{1,2} 

¹ Center for Ecological Research, Northeast Forestry University, Harbin 150040, China; ecology_liufan@nefu.edu.cn (F.L.); wangck-cf@nefu.edu.cn (C.W.)

² Key Laboratory of Sustainable Forest Ecosystem Management-Ministry of Education, Northeast Forestry University, Harbin 150040, China

* Correspondence: xcwang_cer@nefu.edu.cn; Tel.: +86-451-82190615

Received: 21 March 2019; Accepted: 2 May 2019; Published: 5 May 2019



Abstract: Near-surface remote sensing is an effective tool for *in situ* monitoring of canopy phenology, but the uncertainties involved in sensor-types and their deployments are rarely explored. We comprehensively compared three types of sensor (i.e., digital camera, spectroradiometer, and routine radiometer) at different inclination- and azimuth-angles in monitoring canopy phenology of a temperate deciduous forest in Northeast China for three years. The results showed that the greater contribution of understory advanced the middle of spring (MOS) for large inclination-angle of camera and spectroradiometer. The length of growing season estimated by camera from the east direction extended 11 d than that from the north direction in 2015 due to the spatial heterogeneity, but there was no significant difference in 2016 and 2018. The difference in field of view of sensors caused the MOS and the middle of fall, estimated by camera, to lag a week behind those by spectroradiometer and routine radiometer. Overall, the effect of azimuth-angle was greater than that of inclination-angle or sensor-type. Our assessments of the sensor types and their deployments are critical for the long-term accurate monitoring of phenology at the site scale and the regional/global-integration of canopy phenology data.

Keywords: digital camera; spectroradiometer; radiometer; inclination angle; azimuth; uncertainty

1. Introduction

Global climate warming advances the spring phenology [1–3], delays the autumn phenology [4,5], and consequently extends the length of growing season (LOS) of temperate and boreal forests. The extended LOS remarkably affects the CO₂ flux in forest ecosystems [6,7], with one-day extension in LOS leading to an increase in gross primary productivity of 5.8 gC m^{−2} yr^{−1} (0.6%) [8]. Therefore, accurately monitoring vegetation phenology is critical for modeling the carbon cycling of terrestrial ecosystems [9–11].

Currently, vegetation phenology is monitored with three major methods: ground observation, satellite, and near-surface remote sensing. The traditional ground observation usually records specific phenology events (e.g., budburst, leaf-out, coloration, defoliation) for a few individuals within a community [12], while the satellite remote sensing (e.g., MODIS) is normally performed at a large scale with difficulty of identifying the spatial heterogeneity within pixels [13]. Nevertheless, the near-surface remote sensing, with moderate spatial representation and high temporal resolution, bridges the ground observation and satellite remote sensing and thus provides an effective approach for long-term and continuous *in situ* monitoring canopy phenology [14,15]. The phenology networks of near-surface

remote sensing (e.g., the phenocam network, specnet, and FLUXNET) provide a data-sharing platform for observing the phenology of terrestrial ecosystems [16–18]. However, long-term and continuous monitoring of canopy phenology at a specific site and regional/global-scale syntheses of the data across sites are seriously hindered due to various sensor-types and deployments used [16,17,19,20]. Assessing the potential discrepancies among multi-sourced data of phenology and the uncertainty will improve the accuracy of phenology estimates at both local and regional scales [16,21,22].

When using the near-surface remote sensing technique, canopy phenology is often characterized by the vegetation index (VI, the color index with digital camera is also considered as VI for convenience) calculated from the reflectance or digital number (DN) measured with three types of sensor: the narrowband VI with spectroradiometer (VI_N), the broadband VI with radiometers (VI_B) and the color index with digital camera (VI_C). The viewing-angle effect of each type of sensor should be first tackled in syntheses of the phenology data [23]. Ideally, camera is inclined downward 20–40° to broaden the field of view (FOV) and include some sky to avoid dark images [24]. But such a near-horizontal view may affect the VI_C and the phenophases via the bidirectional reflectance [25,26], and the oblique angle produces a greater effective leaf area and might lead to an earlier peak of VI_C [27]. Conversely, a vertical view can capture more understory phenology [20,28], but it reduces the FOV [29] and is susceptible to the tower-structure [30–32]. However, the effect of camera inclination-angle on phenophases and its uncertainty are seldom assessed [30]. Similarly, few studies investigated the effects of inclination-angles of spectroradiometer and routine radiometers on VI_N and VI_B [33,34].

The azimuth-angle of a sensor may also introduce uncertainties in monitoring canopy phenology due to the spatial heterogeneity [35,36]. Most cameras are installed northward in order to reduce lens flare and canopy shadows [15], but some cameras are facing other directions for monitoring specific species or minimizing limitations of the local terrains [37]. Clearly, the effects of sensor azimuth-angle on tower-based VI and phenophases need more investigations.

Sensor-type is critical to integrate phenology data across sites, but few studies have investigated the effect of sensor-type on the VI seasonality and phenophases. Richardson et al. [38] reported that the green chromatic coordinate measured with a digital camera (GCC_C) proceeded more slowly than broadband normalized difference vegetation index measured with radiometers ($NDVI_B$); Saitoh et al. [39] found that the VI_N was linearly correlated with the VI_C , but did not report the effect of sensor-type on the phenophases. Thus, a systematic comparison among sensor-types is urgent for integrating phenology data from multi-sites with different sensors.

In this study, we assessed the effects of sensor types and their deployments on canopy phenology of a temperate broadleaved deciduous forest at the Maoershan eddy flux site in Northeast China. Specially, we compared the VI and phenophases derived from different inclination- and azimuth-angles of three types of sensor (i.e., digital camera, spectroradiometer, and radiometer), which would provide some guidelines for *in situ* monitoring canopy phenology of terrestrial ecosystems at both local and global network platforms.

2. Materials and Methods

2.1. Study Area

The study was conducted at the Maoershan Forest Ecosystem Research Station of Northeast Forestry University, Heilongjiang Province, Northeast China (45°24'N, 127°40'E, 400 m a.s.l.). The climate is a continental monsoon climate. The annual average temperature is 3.1 °C, and the average annual precipitation is 629 mm (1989–2009). The eddy flux tower was established on the northwest-facing (~296°) slope in a temperate broadleaved deciduous forest, with an average slope of ~9°. The wind direction above the canopy is preferentially up-valley (northeast) in the daytime and down-valley (southwest) in the nighttime [40]. The tower is 48 m high, and the dominant canopy is ~20 m high. The overstory of the forest is dominated by *Ulmus japonica*, *Fraxinus mandshurica*, and *Betula platyphylla*, followed by *Betula costata*, *Juglans mandshurica*, *Acer mono*, and *Populus ussuriensis*; the shrubs are

dominated by *Synga reticulata* var. *mandshurica* [41]. The tree biomass was 154 Mg ha^{-1} ; and the maximum leaf area index estimated with the litterfall collection method was $6.5 \text{ m}^2 \text{ m}^{-2}$ for the period of 2008–2017 (Liu et al., unpublished data), of which the understory contributed to 27% [40].

2.2. Field Measurements

2.2.1. Digital Camera Measurements

The canopy images from four azimuth-angles (east, south, west, and north) with an inclination-angle of 30° and four inclination-angles (15° , 30° , 45° , and 60°) in the north direction were manually collected using a digital camera (Coolpix L120, Nikon Corporation, Japan) on the top of the eddy flux tower (48 m above the ground). Seven tripod heads (each in the east, south, and west directions, and four in the north direction) were installed to ensure the position of camera stable for each measurement. The images were collected once every 2–5 d during the leaf unfolding (May–June) and defoliation (September–October) periods, and weekly from July to August for three years (2015, 2016, 2018). All images were collected around noon (11:30–12:00 local time) on sunny or cloudy days. The white balance of camera was set to the sunny mode [30,42,43]. The optical sensor in the camera was a CCD image sensor set with the auto mode of exposure; and all images were stored in JPEG format with a resolution of 4320×3240 .

2.2.2. Spectroradiometer Measurements

The canopy reflectance was manually collected on the tripod heads with four azimuth-angles (east, south, west, and north) and four inclination-angles (15° , 30° , 45° , and 60°) in the north direction using the fiber of FieldSpec 4 with a 25° field angle (Analytical Spectral Devices Inc., Boulder, Colorado, USA). The frequency of data-collecting was synchronized with the camera. The spectral range of spectroradiometer was 350–2500 nm at 1-nm increments. Before every measurement, we optimized the light source of the instrument, and then collected the dark current and measured down-welling radiance by a white Spectralon (Opti-Sciences, Hudson, New Hampshire, USA). The relative reflectance is computed by dividing the energy reflected from the canopy by the energy reflected off the white reference panel (Spectralon). The white reference is a material with approximately 100% reflectance across the entire spectrum. Three spectral curves for each measurement were stored and their average was used as the measurement.

2.2.3. Radiometer Measurements

A net radiometer (CNR4, Kipp & Zonen, the Netherlands) was installed at the top of the flux tower (48 m above ground) to measure incoming and outgoing radiations (W m^{-2}), including solar (shortwave, 300–2800 nm) and long-wave radiations ($4.5\text{--}42 \mu\text{m}$). A pair of photosynthetically active radiometers (400–700 nm, PAR) (PQS1 or PARLITE, Kipp & Zonen, the Netherlands) was also installed to measure the incident and reflected photosynthetic photon flux densities ($\mu\text{mol m}^{-2} \text{ s}^{-1}$). All radiometers were installed horizontally facing downward (i.e., with a 90° of the inclination-angle). Another group of radiometers was added in 2016 that was slope-parallel (i.e., with an 81° of the inclination-angle) and operated for the whole year. All the radiation data were sampled every 5 s and stored 30 min mean in dataloggers (CR1000, Campbell, Scientific, Inc., Logan, UT, USA).

2.3. Data Analysis

2.3.1. Vegetation Index from Digital Camera

The “Phenopix” package with R 3.3.2 was used to select the region of interest (ROI) from the image [44]. We defined two ROIs (one is a large FOV covering most of the entire image, the other matched the FOV of spectroradiometer) to extract the average digital numbers (DN) of the red, green and blue channels of all pixels in the two ROIs respectively, then calculated the GCC_C (Equation (1)) based

on the three channel DN values for each image. All data were used to estimate the phenophases, because the GCC_C suppressed the effect of the illumination conditions [19].

$$GCC_C = \frac{G}{R + G + B} \quad (1)$$

where R, G, and B represent the DN values of red, green, and blue channels, respectively.

2.3.2. Vegetation Index from Spectroradiometer

The reflectance data were extracted from the spectral curve with ViewSpecPro version 5.6. We used the mean reflectance of the three spectral curves to calculate the narrowband normalized difference vegetation index ($NDVI_N$, Equation (2)) (red: 620–670 nm, near-infrared: 841–876 nm). To explore the effects of FOV and spectral resolution of sensors on phenophases (see Section 3.3), we also calculated the GCC_N (Equation (3)) and $NDVI_B$ (Equation (4)) using the similar bands as camera (red: 575–710 nm, green: 510–570 nm, blue: 430–515 nm) and radiometers (PAR: 400–700 nm, near-infrared: 700–2500 nm). Although the maximum wavelength of spectroradiometer (2500 nm) was not exactly consistent with that of CNR4 radiometer (2800 nm), the radiation in 2500–2800 nm may be neglected due to its minimal contribution to the whole near-infrared waveband. The outliers measured on partly cloudy days were excluded to smooth the time series of VI_N .

$$NDVI_N = \frac{r_{nir} - r_{red}}{r_{nir} + r_{red}} \quad (2)$$

$$GCC_N = \frac{r_{green}}{r_{red} + r_{green} + r_{blue}} \quad (3)$$

where r_{nir} , r_{red} , r_{green} , and r_{blue} represent the reflectance of near-infrared, red, green, and blue bands, respectively.

2.3.3. Vegetation Index from Radiometer

To calculate the incident and reflected near-infrared radiation, the PAR was subtracted from the solar (shortwave) radiation for both incident and reflected radiation. Because the unit of PAR ($\mu\text{mol m}^{-2} \text{s}^{-1}$) was different from that of the solar (shortwave) radiation (W m^{-2}), we converted the photosynthetic photon flux density to the energy flux density with the conversion coefficients (the incident coefficient $0.2195 \text{ J } \mu\text{mol photon}^{-1}$, and the reflected coefficient $0.2072 \text{ J } \mu\text{mol photon}^{-1}$) [45]. Then the hemispheric reflectance (albedo) of near-infrared band was obtained as the reflected divided by the incident radiation. The $NDVI_B$ for routine radiometer [46] was calculated by Equation (4). The noise of $NDVI_B$ was smoothed by a moving window approach that assigns the 50th percentile of the values around noon (10:00–14:00 local time) within a 3-d window to the center day [47,48].

$$NDVI_B = \frac{r_{nir} - r_{par}}{r_{nir} + r_{par}} \quad (4)$$

$$r_{par} = \frac{PAR_{out}}{PAR_{in}} \quad (5)$$

$$r_{nir} = \frac{SOLR_{out} - PAR_{out}}{SOLR_{in} - PAR_{in}} \quad (6)$$

where r_{par} and r_{nir} are the albedos of PAR and near-infrared radiation, respectively; PAR_{out} , PAR_{in} , $SOLR_{out}$, and $SOLR_{in}$ are the reflected and incident PAR and solar radiation, respectively.

2.3.4. Phenophase Extraction

The VI from April to June was used to model the seasonal variation in spring by Equation (7) ($12 \leq N \leq 21$). The start, middle, and peak of spring (SOS, MOS, and POS, respectively) were defined as the dates corresponding to the extreme of the curvature change rate (K' , Equation (9)) [49]; and these points were close to 10%, 50%, and 90% of the amplitude, respectively (Figure 1a).

$$f(t) = a + \frac{b}{1 + e^{c+dt}} \quad (7)$$

$$K = \frac{f''(t)}{(1 + f'(t)^2)^{3/2}} \quad (8)$$

$$K' = d^3 a z \left\{ \frac{3z(1-z)(1+z)^3 [2(1+z)^3 + d^2 a^2 z]}{[(1+z)^4 + (daz)^2]^{\frac{5}{2}}} - \frac{(1+z)^2 (1+2z-5z^2)}{[(1+z)^4 + (daz)^2]^{\frac{3}{2}}} \right\} \quad (9)$$

where $f(t)$ is the fitted function; t is the day of year (DOY); a is the minimum of VI in spring, b is the amplitude of VI; c and d control the inflection point and the rate of increase of VI, respectively; K is the curvature of $f(t)$, K' is the curvature change rate of $f(t)$; $f'(t)$ and $f''(t)$ are the first and second derivative of $f(t)$, respectively; $z = e^{c+dt}$.

The VI from August to October was used to model the seasonal pattern in fall by Equation (7) ($12 \leq N \leq 17$), where a is the maximum VI in summer, b is the amplitude of VI, c and d control the inflection point and the rate of decrease of VI. The start, middle, and end of fall (SOF, MOF, and EOF) were defined correspondingly (Figure 1b). The length of growing season (LOS) was expressed in two ways: the duration from MOS to MOF (LOS_1) and the duration from SOS to EOF (LOS_2).

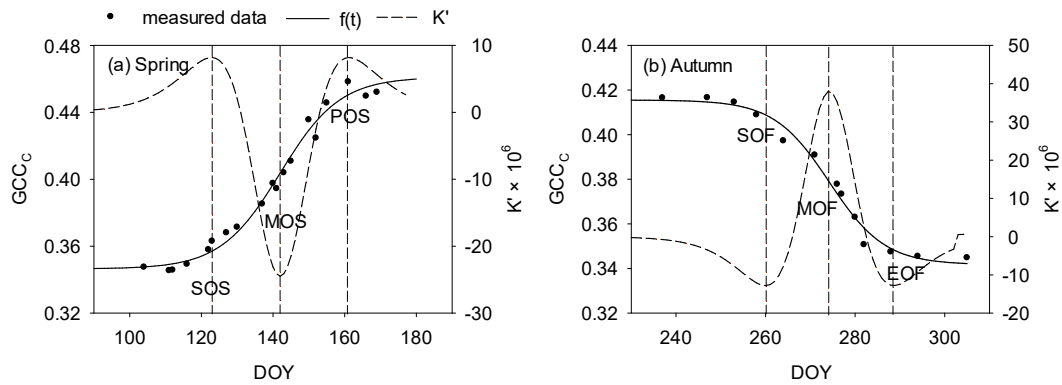


Figure 1. Illustration of the methods used to extract spring (a) and autumn (b) phenophases in the green chromatic coordinate from camera (GCC_c) in 2015. $f(t)$ is the fitted function, K' is the curvature change rate of $f(t)$. SOS: start of spring, MOS: middle of spring, POS: peak of spring, SOF: start of fall, MOF: middle of fall, EOF: end of fall.

2.3.5. Statistical Analysis

The uncertainty of phenophases was calculated as the average width of inner 95% confidence intervals (CI). The significant difference in the phenophases between any two sensors or deployments was given based on the overlapped CI. The high R^2 of all fitted functions (> 0.96) and the relative small confidence interval of phenophases (generally ranged from 1 to 7 d, which was similar to the CI of camera at other sites (0 to 10 d) [50,51]) provided evidence of a high confidence of our results. The spearman's rank correlation [52] was used for evaluating the synchronism of the VI time series measured at different inclination- and azimuth-angles. All statistical analyses were performed by R 3.3.2 or SPSS 19.0, and figures were plotted by Sigmaplot 12.5.

3. Results and Discussion

3.1. Inclination-Angle Effect on the Vegetation Indices and Phenophases

In spring (May–June), both GCC_C and $NDVI_N$ increased with increasing sensor inclination-angle (Figure 2); and the correlation coefficients with the inclination-angle of 15° decreased with increasing inclination-angle (Table 1). In autumn (September–October), however, both VIs almost consistently declined across the four inclination-angles (Figure 2); and the correlation coefficients were close to each other (Table 2). However, the radiometer-orientation had little influence on the $NDVI_B$ (Tables 1 and 2).

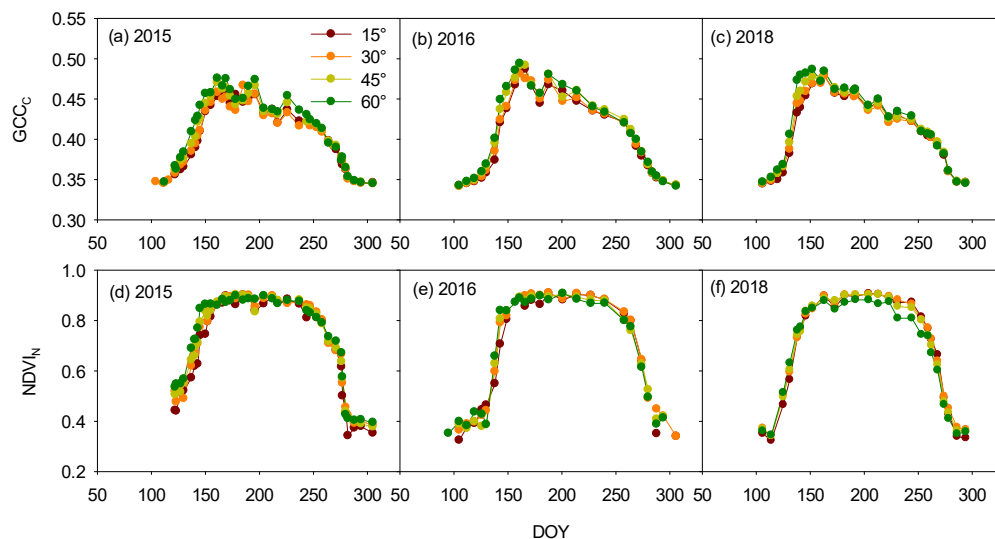


Figure 2. Seasonal variations in the green chromatic coordinate from camera (GCC_C) and the narrowband normalized difference vegetation index from spectroradiometer ($NDVI_N$) at different inclination-angles for the north direction in 2015 (a,d), 2016 (b,e), and 2018 (c,f). DOY: day of year.

Table 1. Spearman’s rank correlations of vegetation indices at different inclination-angles in the north direction.

VI	Inclination Angle	2015		2016		2018	
		Spring	Autumn	Spring	Autumn	Spring	Autumn
GCC_C	30°	0.987	0.993	0.991	1.000	1.000	1.000
	45°	0.982	0.984	1.000	1.000	0.991	1.000
	60°	0.982	0.989	1.000	1.000	0.891	1.000
$NDVI_N$	30°	0.984	0.951	1.000	1.000	1.000	1.000
	45°	0.982	0.945	0.817	1.000	1.000	1.000
	60°	0.973	0.951	0.830	0.964	1.000	0.983
$NDVI_B$	81°			0.980	0.992		

VI: vegetation index; GCC_C : green chromatic coordinate from camera; $NDVI_N$: narrowband normalized difference vegetation index from spectroradiometer; $NDVI_B$: broadband normalized difference vegetation index from routine radiometer. The 15° is the reference for GCC_C and $NDVI_N$, and the 90° is the reference for $NDVI_B$.

The spring phenophases (i.e., SOS, MOS, and POS) of the GCC_C and $NDVI_N$ tended to advance with increasing inclination-angle. The SOS and MOS estimated by GCC_C with 60° inclination were significantly earlier by 12 and 6 d than that with the 15° inclination in 2015, respectively. However, the autumn phenophases (i.e., SOF, MOF, and EOF) did not differ significantly among the four inclination-angles (Table 2). The LOS_2 had much larger uncertainties than did the LOS_1 , although they changed in the same direction with increasing-angle. Notably, the inclination-angle effects of camera and spectroradiometer varied interannually (Table 2).

Table 2. Comparisons of the phenophases (number of days, mean \pm 95% confidence interval) estimated from 30°, 45°, and 60° of inclination-angles with reference to 15° for the north direction in the three measuring years. The comparisons for the radiometer were conducted between 81° and 90°.

VI	Year	Inclination Angle	SOS	MOS	POS	SOF	MOF	EOF	LOS ₁	LOS ₂
GCC _C	2015	30°	0 \pm 5	−1 \pm 2	−1 \pm 5	4 \pm 7	2 \pm 3	1 \pm 7	3 \pm 3	1 \pm 9
		45°	−5 \pm 7	−2 \pm 2	0 \pm 7	0 \pm 8	1 \pm 3	2 \pm 8	3 \pm 4	7 \pm 10
		60°	−12 \pm 8 *	−6 \pm 4 *	−1 \pm 8	−11 \pm 12	−2 \pm 5	6 \pm 12	4 \pm 6	18 \pm 15
	2016	30°	−2 \pm 8	−2 \pm 3	−3 \pm 8	−1 \pm 4	1 \pm 2	3 \pm 4	3 \pm 4	5 \pm 9
		45°	−3 \pm 8	−3 \pm 3	−4 \pm 8	0 \pm 4	1 \pm 2	1 \pm 4	4 \pm 4	4 \pm 9
		60°	−3 \pm 8	−5 \pm 3	−6 \pm 8	−3 \pm 5	1 \pm 2	5 \pm 5	6 \pm 4	8 \pm 10
	2018	30°	0 \pm 5	−1 \pm 2	−3 \pm 5	0 \pm 8	0 \pm 3	0 \pm 8	2 \pm 4	1 \pm 10
		45°	0 \pm 4	−2 \pm 2	−4 \pm 4	0 \pm 8	0 \pm 3	0 \pm 8	2 \pm 4	0 \pm 9
		60°	1 \pm 4	−3 \pm 2 *	−7 \pm 4 *	−2 \pm 9	0 \pm 4	2 \pm 9	3 \pm 4	1 \pm 10
NDVI _N	2015	30°	3 \pm 12	−1 \pm 4	−6 \pm 12	−8 \pm 9	−1 \pm 4	7 \pm 9	0 \pm 6	3 \pm 15
		45°	4 \pm 11	−2 \pm 4	−8 \pm 11	−8 \pm 10	−1 \pm 4	7 \pm 10	1 \pm 6	3 \pm 15
		60°	6 \pm 10	−4 \pm 4	−14 \pm 10 *	2 \pm 7	1 \pm 3	0 \pm 7	5 \pm 5	−6 \pm 12
	2016	30°	7 \pm 12	0 \pm 5	−7 \pm 12	−4 \pm 11	−1 \pm 5	3 \pm 11	−1 \pm 7	−5 \pm 16
		45°	10 \pm 12	−1 \pm 5	−12 \pm 12	−6 \pm 11	−1 \pm 5	4 \pm 11	−1 \pm 7	−6 \pm 16
		60°	12 \pm 12	−1 \pm 5	−14 \pm 12	−3 \pm 11	−2 \pm 5	0 \pm 11	−1 \pm 7	−12 \pm 16
	2018	30°	−3 \pm 7	−1 \pm 3	2 \pm 7	−2 \pm 6	−1 \pm 3	−1 \pm 6	−1 \pm 4	2 \pm 10
		45°	−2 \pm 6	−1 \pm 3	1 \pm 6	−4 \pm 8	−2 \pm 3	−1 \pm 8	−1 \pm 5	2 \pm 10
		60°	−3 \pm 6	−3 \pm 3	−3 \pm 6	0 \pm 8	−1 \pm 3	−2 \pm 8	1 \pm 4	1 \pm 10
NDVI _B	2016	81°	0 \pm 4	0 \pm 2	1 \pm 4	1 \pm 11	−2 \pm 5	−5 \pm 11	−2 \pm 6	−5 \pm 12

VI: vegetation index, GCC_C: green chromatic coordinate from camera, NDVI_N: narrowband normalized difference vegetation index from spectroradiometer. NDVI_B: broadband normalized difference vegetation index from routine radiometer. SOS: start of spring, MOS: middle of spring, POS: peak of spring, SOF: start of fall, MOF: middle of fall, EOF: end of fall, LOS₁: the duration from MOS to MOF, and LOS₂: the duration from SOS to EOF. * indicates significant differences from that from 15° inclination. The positive and negative numbers represent a delay and advance, respectively.

The effect of inclination-angle and its interannual fluctuation might be attributed to the effect of the tree species composition and understory in the FOV of sensors with different inclination-angles or the bidirectional reflectance [30,36]. For camera, the FOV ranged from 1100 (60°) to >90,000 m² (15°). When the comparison among different inclination-angles was constrained in the same area in the images, the effect of inclination-angle on phenophases (Table 3) was generally consistent with the original results (Table 2), suggesting similar tree species composition in different FOVs. In spring, ground vegetation greened-up first, followed by shrubs, and trees last (Liu and Wang, personal observations) [53]. The understory in the FOV of camera from smaller inclination-angle was sheltered more by the layer of tree branches [20,29]. The contribution of the understory to the GCC_C increased with increasing inclination-angle, and thus resulted in earlier SOS, MOS, and POS for larger angles [20]. The radiative transfer model also illustrated that the presence of non-photosynthetic elements reduced the visibility of green vegetation from an oblique viewing angle [29]. Similarly, the spring green-up date of GCC_C with a vertical view was 5 d earlier than that with a horizontal view in the Alice Holt Forest [30]. For spectroradiometer, the FOV ranged from 190 (60°) to 1200 m² (15°), and the NDVI_N with larger inclination-angle had a later SOS in 2015 and 2016 (Table 2). However, it is difficult to distinguish the effects of tree species composition, understory and bidirectional reflectance. The autumn phenology of understory and overstory converged (Liu and Wang, personal observations), thus the VI and three autumn phenophases among four inclination-angles converged as well (Figure 2, Tables 1 and 2).

Table 3. Comparisons of the phenophases (number of days, mean \pm 95% confidence interval) estimated from 30°, 45°, and 60° of inclination-angles with reference to 15° in the three measuring years. The fields of view by green chromatic coordinate from camera were constrained in the same area for all images.

Year	Inclination Angle	SOS	MOS	POS	SOF	MOF	EOF	LOS ₁	LOS ₂
2015	30°	-1 \pm 7	2 \pm 2	2 \pm 7	0 \pm 11	0 \pm 5	0 \pm 11	-2 \pm 5	-1 \pm 13
	45°	-3 \pm 11	3 \pm 3	8 \pm 11	-3 \pm 12	-1 \pm 4	1 \pm 12	-4 \pm 6	3 \pm 16
	60°	-10 \pm 10	-1 \pm 3	8 \pm 10	-2 \pm 17	-1 \pm 6	1 \pm 17	0 \pm 7	10 \pm 19
2016	30°	2 \pm 13	-1 \pm 6	-4 \pm 13	0 \pm 8	0 \pm 3	0 \pm 8	1 \pm 7	-1 \pm 15
	45°	-1 \pm 11	-2 \pm 5	-4 \pm 11	0 \pm 8	1 \pm 3	2 \pm 8	3 \pm 6	2 \pm 13
	60°	-1 \pm 11	-3 \pm 5	-4 \pm 11	0 \pm 9	1 \pm 4	3 \pm 9	4 \pm 6	4 \pm 14
2018	30°	0 \pm 8	0 \pm 3	0 \pm 8	-1 \pm 9	0 \pm 3	0 \pm 9	0 \pm 5	1 \pm 12
	45°	1 \pm 7	-1 \pm 3	-3 \pm 7	0 \pm 8	0 \pm 3	1 \pm 8	2 \pm 4	0 \pm 11
	60°	0 \pm 7	-2 \pm 3	-5 \pm 7	0 \pm 11	1 \pm 4	2 \pm 11	3 \pm 5	2 \pm 13

SOS: start of spring, MOS: middle of spring, POS: peak of spring, SOF: start of fall, MOF: middle of fall, EOF: end of fall, LOS₁: the duration from MOS to MOF, and LOS₂: the duration from SOS to EOF. The positive and negative numbers represent a delay and advance, respectively.

In addition, the GCC_C reached a peak in late spring, which was much earlier than the peak of LAI [54]. Keenan et al [27] thought that the small inclination-angle increased the effective leaf area, thus, the GCC_C maturely saturated. However, we found the larger inclination-angle resulted in an earlier POS (Table 2), indicating that increasing the inclination-angle did not delay the peak of GCC_C. The reason for the summer decline of GCC_C after the POS and the physiological mechanism of POS are poorly understood and need further exploration [55–58].

Currently, most camera-phenology studies adopt near-horizontal inclination-angles (0–25°), partly because most flux towers are not high enough (< 15 m) to broaden the FOV [59]. For example, assuming the camera is mounted at 15 m above the canopy, the FOV with nadir view for 45° of the view-angle of the StarDot NetCam is only 120 m², much smaller than 2700 m² for the inclination-angle of 30° [30]. Such a small FOV is difficult to match the climatic footprint of eddy fluxes or the pixel area of satellite images. In addition, we also need to distinguish differences in the phenology between overstory and understory with multi-cameras [28,60], because of their difference in response to climate change [61].

3.2. Azimuth-Angle Effect on the Vegetation Indices and Phenophases

The GCC_C and NDVI_N in the east, south and west directions related differently to the equivalents in the north direction, indicating diverse seasonal amplitudes between the four azimuths (Figure 3, Table 4).

Table 4. Spearman's rank correlations of vegetation indices at different azimuth-angles with an inclination angle of 30°.

VI	Azimuth Angle	2015		2016		2018	
		Spring	Autumn	Spring	Autumn	Spring	Autumn
GCC _C	E	0.970	0.993	0.991	1.000	0.745	1.000
	S	0.994	0.974	1.000	0.986	0.945	0.967
	W	0.997	1.000	0.991	1.000	0.955	0.983
NDVI _N	E	0.951	0.991	0.976	1.000	0.855	1.000
	S	0.956	0.965	0.988	0.976	0.855	1.000
	W	0.979	0.996	0.952	1.000	0.900	0.983

VI: vegetation index, GCC_C: green chromatic coordinate from camera, NDVI_N: narrowband normalized difference vegetation index from spectroradiometer. E, S, and W stand for east, south, and west, respectively. The north is the reference.

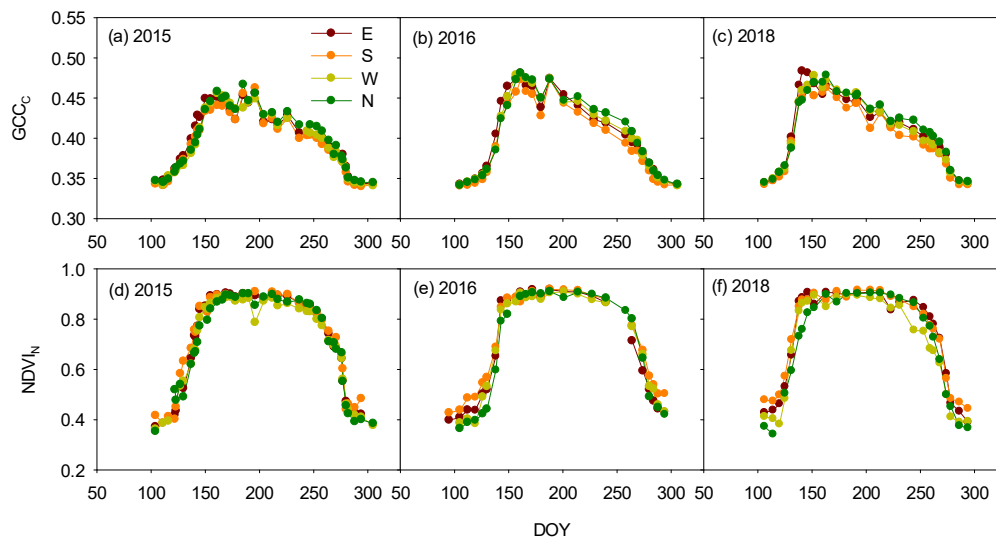


Figure 3. Seasonal variations in the green chromatic coordinate from camera (GCC_C) and narrowband normalized difference vegetation index from spectroradiometer ($NDVI_N$) at different azimuths with an inclination-angle of 30° in 2015 (a,d), 2016 (b,e), and 2018 (c,f). E, S, W, and N stand for east, south, west, and north direction, respectively.

The effect of azimuth-angle on phenophases varied interannually. Compared with the north direction, in 2015, the SOS derived by GCC_C for the east and south directions advanced 12 and 17 d, respectively; the MOS advanced 8 and 7 d; the LOS_1 extended 11 and 9 d, and the LOS_2 elongated 16 and 18 d, respectively (Table 5). The MOS from $NDVI_N$ for the north direction was 7 d later than that for the other three azimuths in 2015 (Table 5). However, there were no significant differences in both GCC_C and $NDVI_N$ between azimuths in 2016 and 2018 (Table 5).

Table 5. Comparisons of the phenophases (number of days, mean \pm 95% confidence interval) estimated from east (E), south (S), and west (W) directions with reference to north (N) with an inclination-angle of 30° in the three measuring years.

VI	Year	Azimuth Angle	SOS	MOS	POS	SOF	MOF	EOF	LOS_1	LOS_2
GCC_C	2015	E	$-12 \pm 6^*$	$-8 \pm 3^*$	-4 ± 6	1 ± 12	2 ± 5	4 ± 12	$11 \pm 5^*$	16 ± 13
		S	$-17 \pm 7^*$	$-7 \pm 3^*$	3 ± 7	2 ± 10	1 ± 4	1 ± 10	9 ± 5	18 ± 13
		W	-6 ± 7	-2 ± 2	3 ± 7	-7 ± 13	-1 ± 5	5 ± 13	1 ± 5	11 ± 14
	2016	E	0 ± 6	$-4 \pm 3^*$	-9 ± 6	-4 ± 9	2 ± 3	8 ± 9	6 ± 4	7 ± 11
		S	0 ± 7	-2 ± 3	-5 ± 7	-7 ± 13	-2 ± 5	2 ± 13	0 ± 6	2 ± 15
		W	2 ± 6	-1 ± 2	-4 ± 6	-1 ± 8	1 ± 3	3 ± 8	2 ± 4	1 ± 10
	2018	E	2 ± 5	-1 ± 2	-4 ± 5	1 ± 10	1 ± 4	1 ± 10	2 ± 4	-1 ± 11
		S	1 ± 5	-2 ± 2	-4 ± 5	2 ± 8	0 ± 3	-2 ± 8	1 ± 4	-3 ± 9
		W	1 ± 5	0 ± 2	-1 ± 5	-3 ± 10	-1 ± 4	2 ± 10	-1 ± 4	1 ± 11
$NDVI_N$	2015	E	-3 ± 8	$-5 \pm 3^*$	-7 ± 8	-3 ± 11	0 ± 5	2 ± 11	4 ± 6	5 ± 14
		S	-10 ± 10	$-9 \pm 4^*$	-7 ± 10	1 ± 13	0 ± 6	-2 ± 13	8 ± 7	8 ± 16
		W	-10 ± 9	$-6 \pm 3^*$	-1 ± 9	0 ± 10	1 ± 4	1 ± 10	6 ± 5	11 ± 14
	2016	E	-2 ± 7	-2 ± 3	-2 ± 7	-11 ± 10	-4 ± 4	2 ± 10	-2 ± 5	5 ± 12
		S	-6 ± 7	-3 ± 3	0 ± 7	-4 ± 12	-2 ± 5	-1 ± 12	1 ± 6	6 ± 14
		W	-6 ± 6	-4 ± 3	-1 ± 6	-1 ± 12	0 ± 5	2 ± 12	4 ± 6	8 ± 13
	2018	E	8 ± 6	-1 ± 3	-10 ± 6	5 ± 7	2 ± 3	0 ± 7	3 ± 4	-8 ± 9
		S	6 ± 6	-2 ± 3	-10 ± 6	7 ± 6	2 ± 3	-3 ± 6	4 ± 4	-9 ± 8
		W	7 ± 6	-2 ± 3	-10 ± 6	4 ± 9	1 ± 4	-2 ± 9	2 ± 5	-9 ± 11

VI: vegetation index, GCC_C : green chromatic coordinate from camera, $NDVI_N$: narrowband normalized difference vegetation index from spectroradiometer. SOS: start of spring, MOS: middle of spring, POS: peak of spring, SOF: start of fall, MOF: middle of fall, EOF: end of fall, LOS: length of growing season. LOS_1 : the duration from MOS to MOF, and LOS_2 : the duration from SOS to EOF. * indicates significant differences with the north sector. The positive and negative numbers represent a delay and advance, respectively.

The differences in the VIs seasonality and phenophases between the four azimuths and the interannual variation were partly attributed to spatial variations in tree species composition, understory and local topography. First, our forest stand is composed of various tree species with divergent phenology along the slope due to microhabitat adaptation. The leaf-onset differed among the tree species, which can consequently result in the azimuth effect. Even for the same species, the spring phenology at the lower slope may be later than that at the upper slope, because the temperature is normally lower near the valley-bottom or toe-slope [50,62–64], which is related to the thermal inversion of the nocturnal boundary layer at our site [40]. Second, the divergence of phenology between overstory and understory can also introduce an azimuth effect. Facing the down-slope may “see” more understory than the upper-slope because of less occlusion of tree branches. Third, the different responses to interannual climate perturbation among various tree species or between overstory and understory can result in the interannual fluctuation of the azimuth effect [65]. Although the effects of shadows, lens, and forward scattering can be minimized by facing north [66], it may need to use multi-sensors towards different directions to ensure the FOV of the phenological sensors to match satellite pixels or EC climatic-footprint [25]. If only one sensor is used, it should point to the prevailing wind direction as far as possible besides considering the species composition and local topography [32]. However, the sun’s direction at solar noon (the true south) should be avoided because the images would be contaminated by direct sunlight [67].

3.3. Sensor-Type Effect on the Vegetation Indices and Phenophases

The seasonal patterns of the VIs during the three measuring years varied between the three types of sensor (Figure 4). Both $NDVI_N$ and $NDVI_B$ reached a plateau from June to mid-August, whereas GCC_C showed a significant peak in early June. The SOS of GCC_C from camera was 14 d later than that of $NDVI_B$ from routine radiometer in 2015 and 4 d later than that of $NDVI_N$ from spectroradiometer in 2018. The MOS estimated by GCC_C from camera was 3–7 d later than that from spectroradiometer and routine radiometer in 2015 and 2016 (Table 6). The SOF and MOF of camera were 18 d and 8 d later than that of radiometer in 2018, respectively.

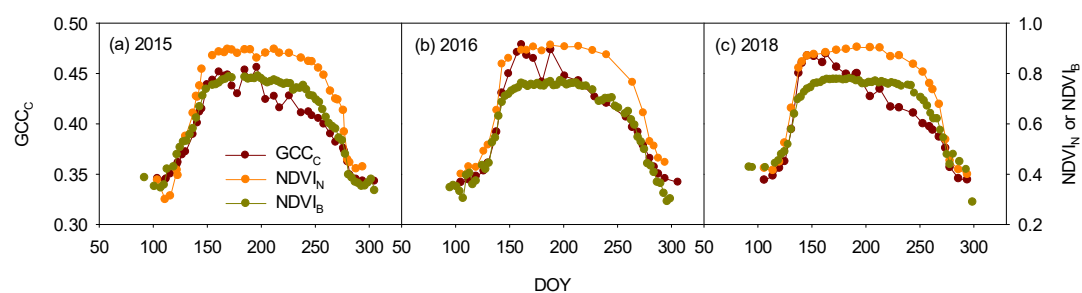


Figure 4. Seasonal variations in the vegetation indices measured with the three types of sensor in 2015 (a), 2016 (b), and 2018 (c). GCC_C : green chromatic coordinate from camera, $NDVI_N$: narrowband normalized difference vegetation index from spectroradiometer, $NDVI_B$: broadband normalized difference vegetation index from routine radiometer. DOY: the day of year. The GCC_C and $NDVI_N$ are the mean values of four azimuths with an inclination-angle of 30° . The $NDVI_B$ is calculated by routine radiometer with an inclination-angle of 90° .

Table 6. Differences (number of days, mean \pm 95% confidence interval) in phenophases between different sensors.

VI	Year	SOS	MOS	POS	SOF	MOF	EOF	LOS ₁	LOS ₂
GCC _C vs. NDVI _N	2015	1 \pm 7	4 \pm 3 *	8 \pm 7	−4 \pm 14	−1 \pm 6	3 \pm 14	−5 \pm 7	1 \pm 16
	2016	2 \pm 6	3 \pm 3 *	5 \pm 6	−5 \pm 9	0 \pm 4	4 \pm 9	−4 \pm 5	2 \pm 11
	2018	4 \pm 3 *	2 \pm 1	−1 \pm 3	4 \pm 8	3 \pm 3	3 \pm 8	2 \pm 3	−2 \pm 8
GCC _C vs. NDVI _B	2015	14 \pm 9 *	7 \pm 3 *	−1 \pm 9	7 \pm 11	3 \pm 5	0 \pm 11	−4 \pm 6	−15 \pm 15
	2016	4 \pm 5	4 \pm 1 *	4 \pm 5	−9 \pm 11	0 \pm 5	9 \pm 11	−4 \pm 6	5 \pm 12
	2018	4 \pm 3	0 \pm 1	−4 \pm 3	18 \pm 8 *	8 \pm 4 *	−3 \pm 8	7 \pm 4 *	−7 \pm 9
NDVI _N vs. NDVI _B	2015	13 \pm 10	2 \pm 4	−8 \pm 10	10 \pm 11	4 \pm 5	−3 \pm 11	1 \pm 6	−16 \pm 14
	2016	2 \pm 6	1 \pm 3	−1 \pm 6	−4 \pm 11	0 \pm 6	5 \pm 11	0 \pm 6	3 \pm 13
	2018	0 \pm 2	−2 \pm 1 *	−3 \pm 2	14 \pm 8 *	4 \pm 3	−6 \pm 8	6 \pm 4	−5 \pm 8

VI: vegetation index, GCC_C: green chromatic coordinate from camera, NDVI_N: narrowband normalized difference vegetation index from spectroradiometer, NDVI_B: broadband normalized difference vegetation index from routine radiometer. SOS: start of spring, MOS: middle of spring, POS: peak of spring, SOF: start of fall, MOF: middle of fall, EOF: end of fall, LOS₁: the duration from MOS to MOF, and LOS₂: the duration from SOS to EOF. * indicates significant differences between sensors. The GCC_C and NDVI_N are the mean values of four azimuths with an inclination-angle of 30°. The NDVI_B is calculated by routine radiometer with an inclination-angle of 90°.

We proposed three potential explanations for the differences in the seasonality of VIs and phenophases estimated by different types of sensor. First, the species composition within the FOV is sensor-specific and thus affects the phenology estimates. At our site, the FOV was in the order of camera (12400 m² for the 30° inclination) > radiometer (9800 m²) > spectroradiometer (4500 m² for the 30° inclination). To further explore the potential effect of FOV, we calculated the NDVI_B of spectroradiometer using the same bands as radiometer to exclude potential spectral mismatch, and found that the SOS and MOS had significant differences (5–23 d) between spectroradiometer and radiometer in 2015 and 2016 (Table 7), suggesting that integrating various sensors should consider the influence of FOV. Second, the difference of biophysical meaning of each VI leads to seasonal asynchrony and different phenophases [31,68–70], which is confirmed by the nonlinear relationship between GCC and NDVI [29]. The GCC is more sensitive to leaf color than leaf area, while NDVI has an advantage in monitoring canopy LAI [31,69]. Similar to our results, the MOS of NDVI_B was 4 d later than that of GCC_C in Bartlett Experimental Forest [38,70]. Finally, the difference in spectral resolutions can cause a discrepancy of phenophases between sensors. We selected the FOV of camera to match that of the spectroradiometer to exclude potential influence of FOV, and compared the differences of phenophases estimates between GCC_N from spectroradiometer and GCC_C from camera. The results showed that there was a slight but non-significant difference in the phenophases between camera and spectroradiometer (Table 7), which is likely related to the slight mismatch of the waveband [24]. Collectively, the variability in FOV may be important for integrating the phenophases from different sensors, especially at heterogeneous sites. Overall, the routine radiometer may be more accurate than the others. Spectroradiometer is sensitive to the weather condition, and thus leads to a slightly larger uncertainty of phenophases (Tables 2 and 5). Camera only measures the reflected DN values and lacks information of incident radiation [31]. Our findings provide some guidelines for *in situ* monitoring canopy phenology of terrestrial ecosystems at both local and global network platforms. However, the effects of sensor type and deployment for other land cover types and potential interannual variations in these effects at the longer time-scale need further investigations.

Table 7. The difference (number of days, mean \pm 95% confidence interval) of phenophases between the same vegetation index measured with different sensors.

VI	Year	SOS	MOS	POS	SOF	MOF	EOF	LOS ₁	LOS ₂
GCC _N vs. GCC _C	2015	1 \pm 7	−2 \pm 3	−5 \pm 7	5 \pm 15	2 \pm 6	−1 \pm 15	4 \pm 6	−2 \pm 16
	2016	1 \pm 5	−3 \pm 2	−6 \pm 5	−3 \pm 11	−1 \pm 4	2 \pm 11	2 \pm 5	1 \pm 12
	2018	−2 \pm 3	0 \pm 2	1 \pm 3	1 \pm 8	0 \pm 3	−1 \pm 8	0 \pm 4	1 \pm 9
NDVI _{BS} vs. NDVI _B	2015	23 \pm 11 *	13 \pm 4 *	3 \pm 11	1 \pm 14	−1 \pm 6	4 \pm 14	−15 \pm 7 *	−27 \pm 18
	2016	12 \pm 5 *	5 \pm 2 *	−2 \pm 5	−15 \pm 17	−5 \pm 7	−4 \pm 17	−10 \pm 7 *	−8 \pm 18
	2018	5 \pm 5	1 \pm 2	−3 \pm 5	8 \pm 10	2 \pm 5	5 \pm 10	1 \pm 5	−10 \pm 11

VI: vegetation index, GCC_C: green chromatic coordinate from digital camera, GCC_N: green chromatic coordinate from the spectroradiometer, NDVI_B: broadband normalized difference vegetation index from routine radiometer, NDVI_{BS}: broadband normalized difference vegetation index from spectroradiometer. SOS: start of spring, MOS: middle of spring, POS: peak of spring, SOF: start of fall, MOF: middle of fall, EOF: end of fall, LOS: length of growing season. LOS₁: the duration from MOS to MOF, and LOS₂: the duration from SOS to EOF. * indicate significant differences between the two sensors. The GCC_C, GCC_N, and NDVI_{BS} are the mean values of four azimuths with an inclination-angle of 30°, the NDVI_B is the calculated by the routine radiometers with an inclination-angle of 90°. The GCC_C and GCC_N were constrained in the same field of view, the NDVI_B and NDVI_{BS} were constrained in the same waveband.

4. Conclusions

We assessed the differences in phenology estimates among three types of sensor and their deployments. The greater contribution of understory advanced the MOS from camera and spectroradiometer with an inclination-angle of 60°. The LOS estimated from camera for the east direction extended 11 d than that for the north direction only in 2015. The effect of azimuth on the phenophases was implicated with spatial variations in tree species composition. The azimuth effect varied interannually perhaps because of the divergent responses of various tree species or of the overstory and understory to the climatic fluctuations. The difference in FOV between sensors was the primary cause that the SOS, MOS, and MOF from camera significantly lagged behind that from spectroradiometer or routine radiometers. Overall, the effect of azimuth-angle was slightly larger than the effect of inclination-angle or sensor-type. These effects should be taken into consideration in both long-term *in situ* monitoring of forest phenology at a single site and/or integrating regional or global phenology data.

Author Contributions: X.W. designed the study, F.L. and X.W. collected the data. F.L. processed the data, and wrote the first draft. All authors contributed to the results, discussion and manuscript writing.

Funding: This research was funded by the Fundamental Research Fund for the Central University (Grant No. 2572018AA15), the Natural Science Foundation of Heilongjiang Province of China (Grant No. QC2017010) and the Program for Changjiang Scholars and Innovative Research Team in University (Grant No. IRT_15R09).

Acknowledgments: We thank the three anonymous reviewers for their valuable comments, and Guangdong Cao, Qing Kong, Yuan Zhu and Yingchi Li for their field assistance.

Conflicts of Interest: The authors declare no conflict of interest.

References

1. Piao, S.L.; Tan, J.G.; Chen, A.P.; Fu, Y.H.; Ciais, P.; Liu, Q.; Janssens, I.A.; Vicca, S.; Zeng, Z.; Jeong, S.-J. Leaf onset in the northern hemisphere triggered by daytime temperature. *Nat. Commun.* **2015**, *6*, 6911. [CrossRef]
2. Menzel, A.; Sparks, T.H.; Estrella, N.; Koch, E.; Aasa, A.; Ahas, R.; ALM-KÜBLER, K.; Bissolli, P.; Braslavská, O.G.; Briede, A. European phenological response to climate change matches the warming pattern. *Glob. Chang. Biol.* **2006**, *12*, 1969–1976. [CrossRef]
3. Schwartz, M.D.; Ahas, R.; Aasa, A. Onset of spring starting earlier across the Northern Hemisphere. *Glob. Chang. Biol.* **2006**, *12*, 343–351. [CrossRef]

4. Estiarte, M.; Peñuelas, J. Alteration of the phenology of leaf senescence and fall in winter deciduous species by climate change: Effects on nutrient proficiency. *Glob. Chang. Biol.* **2015**, *21*, 1005–1017. [[CrossRef](#)]
5. Gill, A.L.; Gallinat, A.S.; Sanders-DeMott, R.; Rigden, A.J.; Gianotti, D.J.S.; Mantooth, J.A.; Templer, P.H. Changes in autumn senescence in northern hemisphere deciduous trees: A meta-analysis of autumn phenology studies. *Ann. Bot.* **2015**, *116*, 875–888. [[CrossRef](#)]
6. Richardson, A.D.; Anderson, R.S.; Arain, M.A.; Barr, A.G.; Bohrer, G.; Chen, G.; Chen, J.M.; Ciais, P.; Davis, K.J.; Desai, A.R. Terrestrial biosphere models need better representation of vegetation phenology: Results from the North American Carbon Program Site Synthesis. *Glob. Chang. Biol.* **2012**, *18*, 566–584. [[CrossRef](#)]
7. Barichivich, J.; Briffa, K.R.; Myneni, R.B.; Osborn, T.J.; Melvin, T.M.; Ciais, P.; Piao, S.; Tucker, C. Large-scale variations in the vegetation growing season and annual cycle of atmospheric CO₂ at high northern latitudes from 1950 to 2011. *Glob. Chang. Biol.* **2013**, *19*, 3167–3183. [[CrossRef](#)]
8. Piao, S.L.; Friedlingstein, P.; Ciais, P.; Viovy, N.; Demarty, J. Growing season extension and its impact on terrestrial carbon cycle in the Northern Hemisphere over the past 2 decades. *Glob. Biogeochem. Cycle* **2007**, *21*, 1148–1154. [[CrossRef](#)]
9. Richardson, A.D.; Keenan, T.F.; Migliavacca, M.; Ryu, Y.; Sonnentag, O.; Toomey, M. Climate change, phenology, and phenological control of vegetation feedbacks to the climate system. *Agric. For. Meteorol.* **2013**, *169*, 156–173. [[CrossRef](#)]
10. Wu, J.; Albert, L.; Lopes, A.; Restrepo-Coupe, N.; Hayek, M.; Wiedemann, K.; Guan, K.; Stark, S.; Christoffersen, B.; Prohaska, N. Leaf development and demography explain photosynthetic seasonality in Amazon evergreen forests. *Science* **2016**, *351*, 972–976. [[CrossRef](#)]
11. Zhang, Y.L.; Song, C.H.; Band, L.E.; Sun, G.; Li, J.X. Reanalysis of global terrestrial vegetation trends from MODIS products: Browning or greening? *Remote Sens. Environ.* **2017**, *191*, 145–155. [[CrossRef](#)]
12. Sparks, T.H.; Menzel, A. Observed changes in seasons: An overview. *Int. J. Climatol.* **2002**, *22*, 1715–1725. [[CrossRef](#)]
13. Ahl, D.E.; Gower, S.T.; Burrows, S.N.; Shabanov, N.V.; Myneni, R.B.; Knyazikhin, Y. Monitoring spring canopy phenology of a deciduous broadleaf forest using MODIS. *Remote Sens. Environ.* **2006**, *104*, 88–95. [[CrossRef](#)]
14. Balzarolo, M.; Vicca, S.; Nguy-Robertson, A.L.; Bonal, D.; Elbers, J.A.; Fu, Y.H.; Grünwald, T.; Horemans, J.A.; Papale, D.; Peñuelas, J. Matching the phenology of net ecosystem exchange and vegetation indices estimated with MODIS and FLUXNET in-situ observations. *Remote Sens. Environ.* **2016**, *174*, 290–300. [[CrossRef](#)]
15. Richardson, A.D.; Klosterman, S.; Toomey, M. Near-surface sensor-derived phenology. In *Phenology: An Integrative Environmental Science*; Springer: Berlin/Heidelberg, Germany, 2013; pp. 413–430.
16. Gamon, J.A.; Rahman, A.F.; Dungan, J.L.; Schildhauer, M.; Huemmrich, K.F. Spectral Network (SpecNet)-What is it and why do we need it? *Remote Sens. Environ.* **2006**, *103*, 227–235. [[CrossRef](#)]
17. Brown, T.B.; Hultine, K.R.; Steltzer, H.; Denny, E.G.; Denslow, M.W.; Granados, J.; Henderson, S.; Moore, D.; Nagai, S.; Sanclements, M. Using phenocams to monitor our changing Earth: Toward a global phenocam network. *Front. Ecol. Environ.* **2016**, *14*, 84–93. [[CrossRef](#)]
18. Richardson, A.D. Tracking seasonal rhythms of plants in diverse ecosystems with digital camera imagery. *New Phytol.* **2018**. [[CrossRef](#)] [[PubMed](#)]
19. Sonnentag, O.; Hufkens, K.; Teshera-Sterne, C.; Young, A.M.; Friedl, M.; Braswell, B.H.; Milliman, T.; O’Keefe, J.; Richardson, A.D. Digital repeat photography for phenological research in forest ecosystems. *Agric. For. Meteorol.* **2012**, *152*, 159–177. [[CrossRef](#)]
20. Liu, Y.; Hill, M.J.; Zhang, X.; Wang, Z.; Richardson, A.D.; Hufkens, K.; Filippa, G.; Baldocchi, D.D.; Ma, S.; Verfaillie, J. Using data from Landsat, MODIS, VIIRS and PhenoCams to monitor the phenology of California oak/grass savanna and open grassland across spatial scales. *Agric. For. Meteorol.* **2017**, *237*, 311–325. [[CrossRef](#)]
21. Garritty, S.R.; Bohrer, G.; Maurer, K.D.; Mueller, K.L.; Vogel, C.S.; Curtis, P.S. A comparison of multiple phenology data sources for estimating seasonal transitions in deciduous forest carbon exchange. *Agric. For. Meteorol.* **2012**, *151*, 1741–1752. [[CrossRef](#)]
22. Anderson, H.; Nilsen, L.; Tømmervik, H.; Karlsen, S.; Nagai, S.; Cooper, E. Using ordinary digital cameras in place of near-infrared sensors to derive vegetation indices for phenology studies of high Arctic vegetation. *Remote Sens.* **2016**, *8*, 847. [[CrossRef](#)]

23. Sonnentag, O.; Detto, M.; Vargas, R.; Ryu, Y.; Runkle, B.; Kelly, M.; Baldocchi, D. Tracking the structural and functional development of a perennial pepperweed (*Lepidium latifolium* L.) infestation using a multi-year archive of webcam imagery and eddy covariance measurements. *Agric. For. Meteorol.* **2011**, *151*, 916–926. [[CrossRef](#)]
24. Richardson, A.D.; Hufkens, K.; Milliman, T.; Aubrecht, D.M.; Chen, M.; Gray, J.M.; Johnston, M.R.; Keenan, T.F.; Klosterman, S.T.; Kosmala, M.; et al. Tracking vegetation phenology across diverse North American biomes using PhenoCam imagery. *Sci. Data* **2018**, *5*, 180028. [[CrossRef](#)]
25. Gamon, J.A. Optical sampling of the flux tower footprint. *Biogeosciences* **2015**, *12*, 4509–4523. [[CrossRef](#)]
26. Balzarolo, M.; Anderson, K.; Nichol, C.; Rossini, M.; Vescovo, L.; Arriga, N.; Wohlfahrt, G.; Calvet, J.-C.; Carrara, A.; Cerasoli, S. Ground-based optical measurements at European flux sites: A review of methods, instruments and current controversies. *Sensors* **2011**, *11*, 7954–7981. [[CrossRef](#)]
27. Keenan, T.F.; Darby, B.; Felts, E.; Sonnentag, O.; Friedl, M.A.; Hufkens, K.; O’Keefe, J.; Klosterman, S.; Munger, J.W.; Toomey, M. Tracking forest phenology and seasonal physiology using digital repeat photography: A critical assessment. *Ecol. Appl.* **2014**, *24*, 1478–1489. [[CrossRef](#)]
28. Moore, C.E.; Beringer, J.; Evans, B.; Hutley, L.B.; Tapper, N.J. Tree-grass phenology information improves light use efficiency modelling of gross primary productivity for an Australian tropical savanna. *Biogeosciences* **2017**, *14*, 1–38. [[CrossRef](#)]
29. Vrieling, A.; Meroni, M.; Darvishzadeh, R.; Skidmore, A.K.; Wang, T.; Zurita-Milla, R.; Oosterbeek, K.; O’Connor, B.; Paganini, M. Vegetation phenology from Sentinel-2 and field cameras for a Dutch barrier island. *Remote Sens. Environ.* **2018**, *215*, 517–529. [[CrossRef](#)]
30. Mizunuma, T.; Wilkinson, M.; Eaton, E.L.; Mencuccini, M.; Morison, J.I.L.; Grace, J. The relationship between carbon dioxide uptake and canopy colour from two camera systems in a deciduous forest in southern England. *Funct. Ecol.* **2013**, *27*, 196–207. [[CrossRef](#)]
31. D’Odorico, P.; Gonsamo, A.; Gough, C.M.; Bohrer, G.; Morison, J.; Wilkinson, M.; Hanson, P.J.; Gianelle, D.; Fuentes, J.D.; Buchmann, N. The match and mismatch between photosynthesis and land surface phenology of deciduous forests. *Agric. For. Meteorol.* **2015**, *214*, 25–38. [[CrossRef](#)]
32. Eklundh, L.; Jin, H.; Schubert, P.; Guzinski, R.; Heliasz, M. An optical sensor network for vegetation phenology monitoring and satellite data calibration. *Sensors* **2011**, *11*, 7678–7709. [[CrossRef](#)] [[PubMed](#)]
33. Matzinger, N.; Andretta, M.; Gorsel, E.V.; Vogt, R.; Ohmura, A.; Rotach, M. Surface radiation budget in an Alpine valley. *Q. J. R. Meteorol. Soc.* **2003**, *129*, 877–895. [[CrossRef](#)]
34. Tittebrand, A.; Spank, U.; Bernhofer, C. Comparison of satellite- and ground-based NDVI above different land-use types. *Theor. Appl. Climatol.* **2009**, *98*, 171–186. [[CrossRef](#)]
35. Hilker, T.; Gitelson, A.; Coops, N.C.; Hall, F.G.; Black, T. Tracking plant physiological properties from multi-angular tower-based remote sensing. *Oecologia* **2011**, *165*, 865–876. [[CrossRef](#)] [[PubMed](#)]
36. Moore, C.E.; Brown, T.; Keenan, T.F.; Duursma, R.A.; Dijk, A.I.J.M.V.; Beringer, J.; Culvenor, D.; Evans, B.; Huete, A.; Hutley, L.B. Australian vegetation phenology: New insights from satellite remote sensing and digital repeat photography. *Biogeosciences* **2016**, *13*, 5085–5102. [[CrossRef](#)]
37. Ahrends, H.E.; Brügger, R.; Stöckli, R.; Schenk, J.; Michna, P.; Jeanneret, F.; Wanner, H.; Eugster, W. Quantitative phenological observations of a mixed beech forest in northern Switzerland with digital photography. *J. Geophys. Res. Biogeosci.* **2008**, *113*, G04004. [[CrossRef](#)]
38. Richardson, A.D.; Jenkins, J.P.; Braswell, B.H.; Hollinger, D.Y.; Ollinger, S.V.; Smith, M.-L. Use of digital webcam images to track spring green-up in a deciduous broadleaf forest. *Oecologia* **2007**, *152*, 323–334. [[CrossRef](#)] [[PubMed](#)]
39. Saitoh, T.M.; Nagai, S.; Saigusa, N.; Kobayashi, H.; Suzuki, R.; Nasahara, K.N.; Muraoka, H. Assessing the use of camera-based indices for characterizing canopy phenology in relation to gross primary production in a deciduous broad-leaved and an evergreen coniferous forest in Japan. *Ecol. Inform.* **2012**, *11*, 45–54. [[CrossRef](#)]
40. Wang, X.C.; Wang, C.K.; Li, Q.L. Wind regimes above and below a temperate deciduous forest canopy in complex terrain: Interactions between slope and valley winds. *Atmosphere* **2015**, *6*, 60–87. [[CrossRef](#)]
41. Liu, F.; Wang, C.K.; Wang, X.C.; Zhang, J.S.; Zhang, Z.; Wang, J.J. Spatial patterns of biomass in the temperate broadleaved deciduous forest within the fetch of the Maoershan flux tower. *Acta Ecol. Sin.* **2016**, *36*, 6506–6519. [[CrossRef](#)]

42. Richardson, A.D.; Braswell, B.H.; Hollinger, D.Y.; Jenkins, J.P.; Ollinger, S.V. Near-surface remote sensing of spatial and temporal variation in canopy phenology. *Ecol. Appl.* **2009**, *19*, 1417–1428. [[CrossRef](#)]
43. Mizunuma, T.; Mencuccini, M.; Wingate, L.; Ogée, J.; Nichol, C.; Grace, J. Sensitivity of colour indices for discriminating leaf colours from digital photographs. *Methods Ecol. Evol.* **2014**, *5*, 1078–1085. [[CrossRef](#)]
44. Filippa, G.; Cremonese, E.; Migliavacca, M.; Galvagno, M.; Forkel, M.; Wingate, L.; Tomelleri, E.; Cella, U.M.D.; Richardson, A.D. Phenopix: A R package for image-based vegetation phenology. *Agric. For. Meteorol.* **2016**, *220*, 141–150. [[CrossRef](#)]
45. Ross, J.; Sulev, M. Sources of errors in measurements of PAR. *Agric. For. Meteorol.* **2000**, *100*, 103–125. [[CrossRef](#)]
46. Huemmrich, K.F.; Black, T.A.; Jarvis, P.G.; McCaughey, J.; Hall, F.G. High temporal resolution NDVI phenology from micrometeorological radiation sensors. *J. Geophys. Res. Atmos.* **1999**, *104*, 27935–27944. [[CrossRef](#)]
47. Hufkens, K.; Friedl, M.; Sonnentag, O.; Braswell, B.H.; Milliman, T.; Richardson, A.D. Linking near-surface and satellite remote sensing measurements of deciduous broadleaf forest phenology. *Remote Sens. Environ.* **2012**, *117*, 307–321. [[CrossRef](#)]
48. Liu, F.; Wang, C.K.; Wang, X.C. Application of near-surface remote sensing in monitoring dynamics of forest canopy phenology. *Chin. J. Appl. Ecol.* **2018**, *29*, 1768–1778.
49. Zhang, X.Y.; Friedl, M.A.; Schaaf, C.B.; Strahler, A.H.; Hodges, J.C.F.; Gao, F.; Reed, B.C.; Huete, A. Monitoring vegetation phenology using MODIS. *Remote Sens. Environ.* **2003**, *84*, 471–475. [[CrossRef](#)]
50. Elmore, A.J.; Guinn, S.M.; Minsley, B.J.; Richardson, A.D. Landscape controls on the timing of spring, autumn, and growing season length in mid-Atlantic forests. *Glob. Chang. Biol.* **2012**, *18*, 656–674. [[CrossRef](#)]
51. Klosterman, S.; Hufkens, K.; Gray, J.; Melaas, E.; Sonnentag, O.; Lavine, I.; Mitchell, L.; Norman, R.; Friedl, M.; Richardson, A. Evaluating remote sensing of deciduous forest phenology at multiple spatial scales using PhenoCam imagery. *Biogeosciences* **2014**, *11*, 4305–4320. [[CrossRef](#)]
52. Delpierre, N.; Guillemot, J.; Dufrêne, E.; Cecchini, S.; Nicolas, M. Tree phenological ranks repeat from year to year and correlate with growth in temperate deciduous forests. *Agric. For. Meteorol.* **2017**, *234–235*, 1–10. [[CrossRef](#)]
53. Augspurger, C.K.; Salk, C.F. Constraints of cold and shade on the phenology of spring ephemeral herb species. *J. Ecol.* **2016**, *105*, 246–254. [[CrossRef](#)]
54. Liu, Z.; Wang, C.; Chen, J.M.; Wang, X.; Jin, G. Empirical models for tracing seasonal changes in leaf area index in deciduous broadleaf forests by digital hemispherical photography. *For. Ecol. Manag.* **2015**, *351*, 67–77. [[CrossRef](#)]
55. Yang, X.; Tang, J.W.; Mustard, J.F. Beyond leaf color: Comparing camera-based phenological metrics with leaf biochemical, biophysical, and spectral properties throughout the growing season of a temperate deciduous forest. *J. Geophys. Res. Biogeosci.* **2014**, *119*, 181–191. [[CrossRef](#)]
56. Wingate, L.; Ogée, J.; Cremonese, E.; Filippa, G.; Mizunuma, T.; Migliavacca, M.; Moisy, C.; Wilkinson, M.; Moureaux, C.; Wohlfahrt, G. Interpreting canopy development and physiology using a European phenology camera network at flux sites. *Biogeosciences* **2015**, *12*, 5995–6015. [[CrossRef](#)]
57. Brown, L.A.; Dasha, J.; Ogotua, B.O.; Richardson, A.D. On the relationship between continuous measures of canopy greenness derived using near-surface remote sensing and satellite-derived vegetation products. *Agric. For. Meteorol.* **2017**, *247*, 280–292. [[CrossRef](#)]
58. Peltoniemi, M.; Aurela, M.; Böttcher, K.; Kolari, P.; Loehr, J.; Hokkanen, T.; Karhu, J.; Linkosalmi, M.; Tanis, C.M.; Metsämäki, S. Networked web-cameras monitor congruent seasonal development of birches with phenological field observations. *Agric. For. Meteorol.* **2018**, *249*, 335–347. [[CrossRef](#)]
59. Nasahara, K.N.; Nagai, S. Review: Development of an in situ observation network for terrestrial ecological remote sensing: The Phenological Eyes Network (PEN). *Ecol. Res.* **2015**, *30*, 211–223. [[CrossRef](#)]
60. Ryu, Y.; Lee, G.; Jeon, S.; Song, Y.; Kimm, H. Monitoring multi-layer canopy spring phenology of temperate deciduous and evergreen forests using low-cost spectral sensors. *Remote Sens. Environ.* **2014**, *149*, 227–238. [[CrossRef](#)]
61. Ge, Q.; Wang, H.; Dai, J. Phenological response to climate change in China: A meta-analysis. *Glob. Chang. Biol.* **2015**, *21*, 265–274. [[CrossRef](#)]
62. Fisher, J.I.; Mustard, J.F.; Vadeboncoeur, M.A. Green leaf phenology at Landsat resolution: Scaling from the field to the satellite. *Remote Sens. Environ.* **2006**, *100*, 265–279. [[CrossRef](#)]

63. Scheifinger, H.; Menzel, A.; Koch, E.; Peter, C.; Ahas, R. Atmospheric mechanisms governing the spatial and temporal variability of phenological phases in central Europe. *Int. J. Climatol.* **2002**, *22*, 1739–1755. [[CrossRef](#)]
64. Fisher, J.I.; Mustard, J.F. Cross-scalar satellite phenology from ground, Landsat, and MODIS data. *Remote Sens. Environ.* **2007**, *109*, 261–273. [[CrossRef](#)]
65. Inoue, T.; Nagai, S.; Saitoh, T.M.; Muraoka, H.; Nasahara, K.N.; Koizumi, H. Detection of the different characteristics of year-to-year variation in foliage phenology among deciduous broad-leaved tree species by using daily continuous canopy surface images. *Ecol. Inform.* **2014**, *22*, 58–68. [[CrossRef](#)]
66. Toomey, M.; Friedl, M.A.; Frolking, S.; Hufkens, K.; Klosterman, S.; Sonnentag, O.; Baldocchi, D.D.; Bernacchi, C.J.; Biraud, S.C.; Bohrer, G. Greenness indices from digital cameras predict the timing and seasonal dynamics of canopy-scale photosynthesis. *Ecol. Appl.* **2015**, *25*, 99–115. [[CrossRef](#)] [[PubMed](#)]
67. Hufkens, K.; Filippa, G.; Cremonese, E.; Migliavacca, M.; D’Odorico, P.; Peichl, M.; Gielen, B.; Hörtnagl, L.; Soudani, K.; Papale, D.; et al. Assimilating phenology datasets automatically across ICOS ecosystem stations. *Int. Agrophys.* **2018**, *32*, 677–687. [[CrossRef](#)]
68. Petach, A.R.; Toomey, M.; Aubrecht, D.M.; Richardson, A.D. Monitoring vegetation phenology using an infrared-enabled security camera. *Agric. For. Meteorol.* **2014**, *195*, 143–151. [[CrossRef](#)]
69. Filippa, G.; Cremonese, E.; Galvagno, M.; Migliavacca, M.; Sonnentag, O.; Hufkens, K.; Ryu, Y.; Humphreys, E.; Umberto, M.D.C.; Richardson, A.D. NDVI derived from IR-enabled digital cameras: Applicability across different plant functional types. *Agric. For. Meteorol.* **2018**, *249*, 275–285. [[CrossRef](#)]
70. Toda, M.; Richardson, A.D. Estimation of plant area index and phenological transition dates from digital repeat photography and radiometric approaches in a hardwood forest in the Northeastern United States. *Agric. For. Meteorol.* **2018**, *249*, 457–466. [[CrossRef](#)]



© 2019 by the authors. Licensee MDPI, Basel, Switzerland. This article is an open access article distributed under the terms and conditions of the Creative Commons Attribution (CC BY) license (<http://creativecommons.org/licenses/by/4.0/>).